



## Investigating the dominant decomposition mechanisms in lithium-ion battery cells responsible for capacity loss in different stages of electrochemical aging

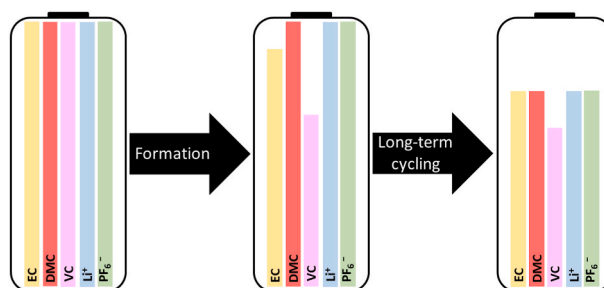
Richard Stockhausen, Lydia Gehrlein, Marcus Müller, Thomas Bergfeldt, Andreas Hofmann, Freya Janina Müller, Julia Maibach, Helmut Ehrenberg, Anna Smith\*

Karlsruhe Institute of Technology (KIT), Institute for Applied Materials (IAM), Hermann-von-Helmholtz-Platz 1, 76344, Eggenstein-Leopoldshafen, Germany

### HIGHLIGHTS

- Consumptions of electrolyte components during cycling are determined in pouch cells.
- Exclusive decomposition of EC and VC is detected during short-term cycling.
- Only minor VC and LiPF<sub>6</sub> decomposition is found during long-term cycling.
- EC and DMC decomposition is dominant during long-term cycling.
- Graphite cracking/Mn in SEI induce electrolyte decompositions upon long-term cycling.

### GRAPHICAL ABSTRACT



### ARTICLE INFO

#### Keywords:

Lithium-ion batteries  
High performance liquid chromatography (HPLC)  
Absolute quantification of electrolyte components  
NCM622  
Graphite  
Pouch cells

### ABSTRACT

Cell aging is a major issue in battery cells, as it affects the application capabilities. The mechanisms contributing to aging and capacity loss are not yet fully understood, so that performance enhancements are difficult to achieve. Here, the decomposition mechanisms responsible for capacity loss in LiNi<sub>0.6</sub>Co<sub>0.2</sub>Mn<sub>0.2</sub>O<sub>2</sub> (NCM622)/graphite lithium-ion pouch cells containing 1 M LiPF<sub>6</sub> in ethylene carbonate (EC)/dimethyl carbonate (DMC) 1:1 by weight with 3 wt% vinylene carbonate (VC) are analyzed. For this purpose, absolute amounts of the electrolyte components are determined in cells at six stages of electrochemical aging using High Performance Liquid Chromatography. The resulting, absolute consumptions of the electrolyte components reveal the dominant degradations. Furthermore, complementary analysis methods, namely X-ray photoelectron spectroscopy, gas chromatography, scanning electron microscopy, energy-dispersive X-ray spectroscopy, and inductively coupled plasma optical emission spectrometry are applied. Two phases of electrochemical aging are identified: During formation and short-term cycling, preferential decomposition of EC and VC is observed accompanied by solid electrolyte interphase (SEI) buildup at the graphite particle edges. During long-term cycling, non-preferential decomposition of each electrolyte component is found associated with SEI growth at edges and basal planes of the graphite particles induced by manganese contamination and/or crack formation in the graphite during de-/lithiation.

\* Corresponding author.

E-mail address: [anna.smith@kit.edu](mailto:anna.smith@kit.edu) (A. Smith).

<https://doi.org/10.1016/j.jpowsour.2022.231842>

Received 19 April 2022; Received in revised form 23 June 2022; Accepted 8 July 2022

Available online 18 July 2022

0378-7753/© 2022 The Authors. Published by Elsevier B.V. This is an open access article under the CC BY-NC-ND license (<http://creativecommons.org/licenses/by-nc-nd/4.0/>).

## 1. Introduction

Among electrochemical energy storage systems, lithium-ion batteries (LIB) offer the highest performance due to their combination of high energy and power densities [1]. Most of the commercially used lithium-ion cells are composed of a layered transition metal oxide cathode, a graphitic carbon anode, a separator, and a liquid electrolyte [2]. This liquid electrolyte usually contains  $\text{LiPF}_6$  as conducting salt, which is dissolved in a mixture of cyclic and linear carbonates, like ethylene carbonate (EC) and dimethyl carbonate (DMC) [2]. Furthermore, various additives (e.g. vinylene carbonate (VC)) can be used to boost the performance of the cells [2]. The key for a further systematic optimization of LIBs is a full understanding of the decomposition processes associated with capacity decay in the battery cells during their lifetime.

In common lithium-ion cells, reductive decomposition of the electrolyte during the first cycles is necessary for their operation. The anode needs to be passivated by forming a surface layer, the solid electrolyte interphase (SEI), as the electrolyte is not stable at the low anode potentials. The SEI is formed on the graphite anode during the first cycles, especially during the first charging, the so-called "formation", by deposition of insoluble reduction products of the electrolyte components [2,3]. The SEI prevents further electrolyte decomposition by blocking electrons, while it is still permeable for lithium-ions, enabling stable cycling [3,4]. VC is a SEI-forming additive that promotes SEI formation and improves the battery cell's performance [5]. VC is preferentially reduced at the graphite anode and suppresses the decomposition of the other electrolyte components [5].

During long-term cycling, transition metals from the cathode, especially manganese, are transferred to the anode [6,7]. The resulting manganese contamination of the SEI deteriorates its passivating properties and promotes further electrolyte decomposition associated with SEI growth and irreversible capacity losses [6–8]. Furthermore, the volume changes of the graphite particles during de-/lithiation can lead to cracks in the graphite particles and consequent ongoing electrolyte decomposition, SEI rebuilding, and irreversible capacity losses [9].

The electrolyte is a key component for lithium-ion cells, as it is in contact with all cell components. Theoretically, the electrolyte decomposition has been studied using molecular dynamics [10,11] or quantum chemistry calculations [12]. Nevertheless, it is crucial to clarify experimentally the decompositions in the electrolyte to refine the models and to gain comprehensive understanding of electrolyte aging. The published, experimental studies about quantitative analyses of electrolytes in lithium-ion cells so far are usually limited to determination of quantity ratios or concentrations. However, concentrations do not contain information about the absolute consumption of the electrolyte components and thus the magnitudes of the electrochemical decompositions remain unknown. Additionally, most of these studies investigated the electrolyte composition at the begin of life (usually after formation) and at the end of life (after a certain number of cycles), although also an investigation of the intermediate stages is of high importance for an accurate understanding of the dominating degradation processes responsible for capacity decay.

In this study,  $\text{LiNi}_{0.6}\text{Co}_{0.2}\text{Mn}_{0.2}\text{O}_2$  (NCM622)/graphite lithium-ion pouch cells with custom-made electrodes are investigated. The electrolyte is extracted from these pouch cells in selected aging steps, namely before formation, after formation, after 25 cycles, after cycling until a remaining capacity of 95%, 90%, and 80% (defined as the end of life). These extracts are subsequently analyzed by High Performance Liquid Chromatography (HPLC) coupled to an electrospray ionization mass spectrometer (ESI/MS) and an ultraviolet/visible light (UV/Vis) detector in order to determine absolute amounts of the electrolyte components in the cells [13]. In addition, the evolved gases are analyzed by gas chromatography (GC), whereas the electrodes are investigated by X-ray photoelectron spectroscopy (XPS), scanning electron microscopy (SEM), energy-dispersive X-ray spectroscopy (EDX), and inductively coupled

plasma optical emission spectrometry (ICP-OES) to obtain a comprehensive insight into the cell aging mechanisms.

The primary aim of this study is to experimentally investigate the magnitudes of the electrochemical decompositions in the electrolyte of pouch cells. The new, experimentally obtained results from this work could be used for further theoretical investigations of the electrolyte decomposition in lithium-ion cells using molecular dynamics.

## 2. Experimental

### 2.1. Cell components

The graphite anodes were composed of a single-sided coating of 93.5 wt% SMG-A5 graphite (Hitachi, Japan), 1.9 wt% Timcal C65 carbon black (Imerys, France), 1.75 wt% sodium carboxymethylcellulose (NaCMC) binder (DuPont, USA), and 2.85 wt% styrene-butadiene rubber (SBR) binder (JSR, Japan) on copper foil with a mass loading of  $7.7 \text{ mg cm}^{-2}$  and a theoretical areal capacity of  $2.7 \text{ mAh cm}^{-2}$ . The final anodes had dimensions of  $5.2 \times 5.2 \text{ cm}$ . The NCM622 cathodes were composed of a single-sided coating of 94 wt% NCM622 (Targray, Canada), 3 wt% polyvinylidene fluoride (PVDF) binder (Solvay, Belgium), 1 wt% Super C65 carbon black (Imerys, France), and 2 wt% Timcal SFG6L graphite (Imerys, France) on aluminum foil and resulting mass loading of  $11.3 \text{ mg cm}^{-2}$  and a theoretical areal capacity of  $1.9 \text{ mAh cm}^{-2}$ . The final cathodes had dimensions of  $5.0 \times 5.0 \text{ cm}$ . The used separators were PET-based and ceramically coated with dimensions of  $5.5 \times 5.5 \text{ cm}$ . Electrode and separator drying was done under reduced pressure for 12 h at  $130 \text{ }^\circ\text{C}$  and  $180 \text{ }^\circ\text{C}$ , respectively.

The electrolyte LP30 + VC was prepared in an argon-filled glovebox (oxygen and water content  $<1 \text{ ppm}$ ). The electrolyte had a water content of  $<20 \text{ ppm}$  determined by Karl Fischer titration. The composition of LP30 + VC is listed in Table 1.

### 2.2. Cell assembly

The cells were assembled in a dry room with a dew point of  $-68 \text{ }^\circ\text{C}$ . In each pouch cell two anodes were placed back to back in the middle, each facing one cathode. Furthermore, two separators were integrated in each cell. Each cell was filled with  $900 \text{ } \mu\text{l}$  of LP30 + VC. After filling, the cells were sealed under reduced pressure. For the calculation of the initial electrolyte mass within the cells, their weight was determined before and after filling and sealing. The capacity of each cells was about 88 mAh.

### 2.3. Cell formation and cycling

Formation and cycling of the cells were performed on a Basytec CTS LAB in a climate chamber with a constant temperature of  $25 \pm 0.1 \text{ }^\circ\text{C}$ . During formation, the cells were charged with 0.1 C until 4.2 V (constant current-constant voltage (CC-CV), until current  $I < 0.05 \text{ C}$ ), then discharged with 0.1 C until 3.0 V (constant current (CC)), subsequently charged again with 0.5 C until 4.2 V (CC-CV, until  $I < 0.05 \text{ C}$ ) and discharged at 0.5 C until 3.0 V (CC). The cells that were analyzed directly after formation were held at 3.0 V for 4 h. Continuous cycling was done with charge at 2 C (CC-CV, until  $I < 0.05 \text{ C}$ ) and discharge at 3 C (CC) in a voltage range of 3.0–4.2 V for various numbers of cycles. For long-term cycling after every 100 cycles, a checkup cycle was performed

**Table 1**  
Composition of the electrolyte LP30 + VC.

Component	Mass fraction [wt%]
EC (Sigma-Aldrich, anhydrous, 99%, USA)	$42.8 \pm 0.1$
DMC (Sigma-Aldrich, anhydrous, $\geq 99\%$ , USA)	$42.8 \pm 0.1$
VC (Gotion, $\geq 99.5\%$ , USA)	$3.00 \pm 0.01$
$\text{LiPF}_6$ (Sigma-Aldrich, battery grade, $\geq 99.99\%$ , USA)	$11.4 \pm 0.1$

where cells were charged with 0.1 C (CC-CV, until  $I < 0.05$  C) and then discharged with 0.1 C (CC). Thereafter, a state of charge (SOC) of 10%, 30%, 50%, 70%, and 90% was set by charging with 0.1 C using the Ah-counter method. At these SOCs the direct current (DC) internal resistances were determined based on current pulses (20 s) of 1 C in discharge direction. The DC internal resistances were calculated by the potential drop and the applied current during the pulses using Ohm's law. After cycling, but before the analyses, the cells were finally charged with 0.1 C until 4.2 V (CC-CV, until  $I < 0.05$  C), discharged with 0.1 C until 3.0 V (CC) and held at 3.0 V for 4 h.

#### 2.4. Electrolyte extraction

The electrolyte was extracted from pouch cells by injecting diethyl carbonate (DEC, Sigma-Aldrich, anhydrous,  $\geq 99\%$ , USA) as diluent. A detailed description of this extraction method can be found in literature [13]. Briefly, 500  $\mu$ l DEC were injected into each pouch cell, followed by a storage of the cell for 14 days to enable a complete mixing of the injected DEC with the original electrolyte. Subsequently, the electrolyte was extracted, filtered by a syringe filter (pore size: 0.45  $\mu$ m), and diluted with acetonitrile (ACN). The DEC injection and the proper extraction were executed in a dry room with a dew point of  $-68$  °C.

#### 2.5. HPLC-UV/Vis and HPLC-ESI/MS conditions

A HPLC system of Nexera XR Ultra High Performance Liquid Chromatograph (Shimadzu, Japan) with an UV/Vis detector (SPD-M20A, Shimadzu, Japan) was used to quantify EC, DMC, DEC, and VC. The column Acclaim 120 C18 (Thermo Fisher Scientific, USA) was utilized with the following characteristics: 250 mm length  $\times$  4.6 mm interior diameter, particle size of 5  $\mu$ m, and pore size of 120 Å. The column oven temperature was 50 °C during the analyses. The wavelength of the UV/Vis detector was set to 190 nm. The flow rate was 1.00 ml min<sup>-1</sup> and the injection volume was 2.0  $\mu$ l for all measurements. The mobile phase was constantly composed of 60% water and 40% ACN (isocratic separation). Each sample was injected three times and the corresponding, average peak area from these three measurements was used for the quantifications.

The same HPLC system coupled with an ESI/MS (LCMS-2020, Shimadzu, Japan) was used for the quantification of Li<sup>+</sup> and PF<sub>6</sub><sup>-</sup>. The column Acclaim 120 C18 (Thermo Fisher Scientific, USA) was used with the following dimensions: 100 mm length  $\times$  3.0 mm interior diameter, particle size of 2.2  $\mu$ m, and pore size of 120 Å. The temperature of the column oven was 50 °C, the flow rate was 0.75 ml min<sup>-1</sup>, and the injection volume was 1.0  $\mu$ l during HPLC-ESI/MS measurements. The composition of the mobile phase during HPLC-ESI/MS measurements is listed in Table S1 in the supplementary information. Furthermore, the nebulizing gas flow was 1.5 l min<sup>-1</sup>, and the drying gas flow was 20.0 l min<sup>-1</sup>. The temperature of the heat block was set to 400 °C, the desolvation line temperature to 300 °C, and the interface temperature to 350 °C. Each solution for the quantification of Li<sup>+</sup> and PF<sub>6</sub><sup>-</sup> was injected four times. Based on the average peak areas from these four measurements per solution, the Li<sup>+</sup> and PF<sub>6</sub><sup>-</sup> concentrations were determined. PF<sub>6</sub><sup>-</sup> was quantified by the PF<sub>6</sub><sup>-</sup> peak itself in the trace of  $m/z = 145.0^-$  u. The quantification of Li<sup>+</sup> was realized by the peak in the trace of  $m/z = 89.1^+$  u. This peak can be ascribed to a complex consisting of Li<sup>+</sup> and two ACN molecules (Li<sup>+</sup>+2 ACN) [13].

Experimental control and measurement data evaluation were done using the software LabSolutions Version 5.97.

#### 2.6. Sample preparation for the HPLC-UV/Vis and HPLC-ESI/MS analyses

The external standard method with a seven-point calibration was used for all the quantifications. The extracted electrolytes and the standard substances were diluted with ACN. The ranges of the mass

fractions of the analytes in the standard samples and the electrolyte-containing samples can be found in Table S2 in the supplementary information. During the sample preparation in a dry room with a dew point of  $-68$  °C, each mass was weighed. Based on these weighed masses, the analytes were quantified.

#### 2.7. GC-TCD conditions and sample preparation for GC-TCD analyses

GC experiments were conducted with a Clarus 690-Arnel GC system (PerkinElmer, USA) equipped with two thermal conductivity detectors (TCD). TotalChrom 6.3.4 software packages were used for data acquisition and data analysis. Gas samples were taken from pouch cells by first injecting 5 ml argon gas into the cells via a syringe (a septum was fixed onto the pouch bag foil) followed by extracting 5 ml of the combined gas from the pouch cell in an argon-filled glovebox (oxygen and water content  $< 1$  ppm). Thereafter, the gas was injected into the gas injection system to load all gas loops of the GC system with the extracted gas. Argon, ethylene (C<sub>2</sub>H<sub>4</sub>), and methane (CH<sub>4</sub>) were detected on the TCD-Arnel GC system. Helium and nitrogen were used as carrier gases for the measurements.

#### 2.8. XPS analyses conditions and sample preparation for XPS analyses

A K-Alpha spectrometer (Thermo Fisher Scientific, UK) was used for the XPS analyses. A microfocused, monochromated Al K <sub>$\alpha$</sub>  X-ray source with 400  $\mu$ m spot size was applied and a pass energy of 50 eV was used. Data acquisition and handling was done by the Thermo Avantage software by Parry et al. [14]. One or more Voigt profiles were used to fit the spectra. For quantification, Scofield sensitivity factors were applied. All spectra were referenced in binding energy to the hydrocarbon C1s peak at 285 eV. Furthermore, the intensity of each spectrum was normalized to its maximum intensity.

For the XPS analyses, the cells were opened, and pieces of the electrodes were cut. Subsequently, the cut electrode pieces were washed by short submersion in 1 ml DMC. Afterwards, the electrode pieces were mounted on a sample holder using conductive copper tape. The sample preparation was conducted in an argon-filled glovebox (oxygen and water content  $< 1$  ppm). Transfer to the spectrometer was done via a transfer module under inert gas conditions.

#### 2.9. ICP-OES conditions and sample preparation for the ICP-OES analyses

The quantification of the elements lithium, manganese, nickel, and cobalt in the electrodes was performed by an iCAP 7600 ICP-OES Duo (Thermo Fisher Scientific, USA). The analysis of the elements was accomplished with four different matrix adapted calibration solutions and an internal standard, namely scandium that was added to each sample with mass fractions of about  $2.00 \cdot 10^{-4}$  wt%. The three major wavelengths of the elements were used for the quantifications. In Table S3 and Table S4 in the supplementary information, the ranges of the mass fractions of the analyzed elements in the samples and the wavelengths used for the quantifications are listed.

The anodes and cathodes extracted from the cells were immersed in DMC for 1 h. The electrodes were weighed afterwards for the eventual calculation of the absolute amounts of the quantified elements. Weighed pieces of the anodes and cathodes with a total weight of about 40–70 mg per cell were subsequently put into aqua regia (6 ml hydrochloric acid subboiled and 2 ml nitric acid subboiled). The aqua regia with the electrodes was stored in a graphite oven at 80 °C for 4 h.

#### 2.10. EDX/SEM conditions and sample preparation for EDX/SEM analyses

A Supra 55 (Carl Zeiss AG, Germany) was utilized for the SEM analyses. An Ultim Extreme detector (Oxford Instruments, UK) with AZtec

software (version 4.2) was used for the EDX analyses. The SEM acceleration voltage was set to 4 kV. The electrodes extracted from the cells were immersed in DMC for 1 h. Pieces of about 0.5 cm<sup>2</sup> were subsequently cut out from the electrodes and mounted on sample holders by conductive tapes. No sputter-coating was applied. Some electrode samples were additionally cross-sectioned by an ion beam milling system (EM TIC 3X, Leica Microsystems GmbH, Germany) using argon ions and an accelerating voltage of 6 kV at 2.2 mA gun current.

### 3. Results and discussion

#### 3.1. Capacity and internal resistance progression

To trace the process of electrochemical aging, the cells are investigated by different analysis methods before formation, after formation, and after different numbers of cycles until a remaining capacity of 80% is reached in this study. In Fig. 1(a), the relative discharge capacity of the analyzed cells cycled at 2 C charge and 3 C discharge until reaching a remaining capacity of 90% and 80% are plotted against the number of cycles. While the capacity decay is pronounced at the beginning of the cycling, it slows down with increasing numbers of cycles, suggesting a deceleration of cell aging at increased numbers of cycles. As the variation of the relative discharge capacity between the cells increase with number of cycles, the longer cycled cells are not analyzed after fixed number of cycles, but after having reached a certain remaining capacity. Thus, it is ensured that the investigated cells have the same aging level.

The DC internal resistances at different SOCs from three of the analyzed cells cycled until a remaining capacity of 80% in dependence on the number of cycles can be seen in Fig. 1(b). In literature, a continuous increase of the internal resistance of lithium-ion cells especially with VC-containing electrolyte with increasing number of cycles and capacity loss, is described [15]. Accordingly, the DC internal resistance rises gradually with number of cycles during prolonged cycling.

#### 3.2. Electrochemical decomposition of the electrolyte

The electrolytes are extracted each from three independent cells, namely before formation (called “fresh”), after formation, after 25 cycles, and after cycling at remaining capacities of 95%, 90%, and 80%. The HPLC analyses of the extracted electrolytes are conducted completely independently of each other on three different days with three times complete sample preparation, for each of the three equally treated cells to check reproducibility. The electrolytes are extracted from the cells by DEC injection that enables not only the determination of the concentrations of the electrolyte components, but also of their absolute amounts of substance in the cell according to literature [13].

The concentrations in the original electrolyte (before DEC injection) are calculated based on the quantified concentrations of DEC, EC, DMC, VC, Li<sup>+</sup>, and PF<sub>6</sub><sup>-</sup> in the extract. DEC, EC, DMC, and VC are quantified by HPLC-UV/Vis, whereas Li<sup>+</sup> and PF<sub>6</sub><sup>-</sup> are quantified by HPLC-ESI/MS. The average concentrations of EC, DMC, VC, Li<sup>+</sup>, and PF<sub>6</sub><sup>-</sup> in the different aging stages are shown in Fig. 2(a). In Fig. 2(b) and (c), the average, relative amounts of substance in the different stages of electrochemical aging are shown. The relative amount of substance is the determined, absolute amount of substance relative to the corresponding, initial amount of substance in the cell. The initial amount of substance in the cell is the concentration in the electrolyte LP30 + VC multiplied with the mass of LP30 + VC filled into the cell during cell assembly. The determined, absolute amounts of substance are calculated by the quantified concentrations of DEC, EC, DMC, VC, Li<sup>+</sup>, and PF<sub>6</sub><sup>-</sup> in the extract, as well as the mass of DEC injected into the cell. Generally, the uncertainties of the relative amounts of substance in Fig. 2(b) and (c) are higher than the uncertainties of the concentrations in Fig. 2(a), as the relative amounts of substance depend on the quantified concentrations with a certain error and the quantified mass of the original electrolyte inside the cell with a certain error. The relative amounts of substance of DMC in the fresh cells are distinctly lower than the expected value of 100% (see Fig. 2(b) and (c)), due to a certain DMC loss during sealing of the cell by vacuum and/or during the extraction itself, as reported in literature [13].

The data in Fig. 2(a) suggest a distinct VC decomposition during formation followed by an almost constant VC concentration during long-term cycling. By contrast, the concentrations of the other components do not show any obvious trends.

Two phases of electrochemical aging can be identified in Fig. 2(c) throughout the lifetime of the pouch cell: During formation and the first 25 cycles in phase I, a fast and distinct decomposition of VC by about 30% can be seen, whereas no significant degradations of the other components are visible. During long-term cycling, meaning from the 26th cycle until the about 800th cycle in phase II, a small deceleration of the VC decomposition is observed (see Fig. 2(c)). The relative amounts of substance of each electrolyte component are reduced slowly in phase II by about 10% (see Fig. 2(c)). The distinction of these two phases of electrochemical aging is confirmed by the coulombic efficiencies of the cells that are shown in Fig. S1 in the supplementary information. The coulombic efficiencies are relatively low during phase I indicating an ongoing SEI buildup after formation during the first about 25 cycles. In phase II, the coulombic efficiencies are higher suggesting a slow SEI growth during long-term cycling.

For an identification of the dominating, electrochemical decomposition mechanisms in the electrolyte it is more informative to consider the absolute amounts of substance decomposed electrochemically. In Fig. 3(a), the average, absolute decomposed amounts of substance of EC,

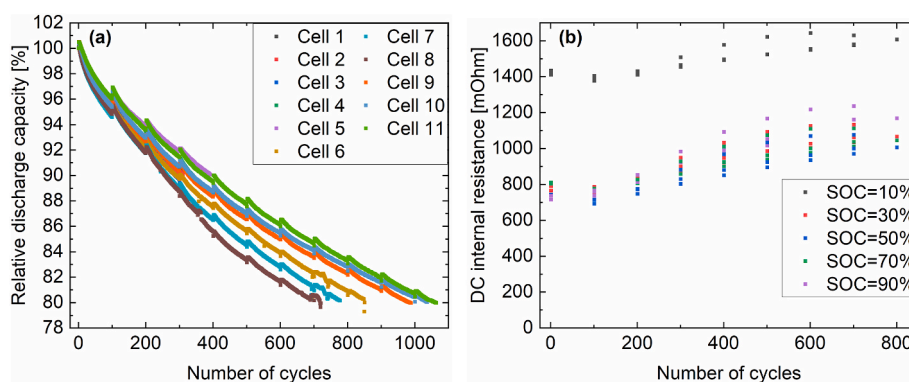
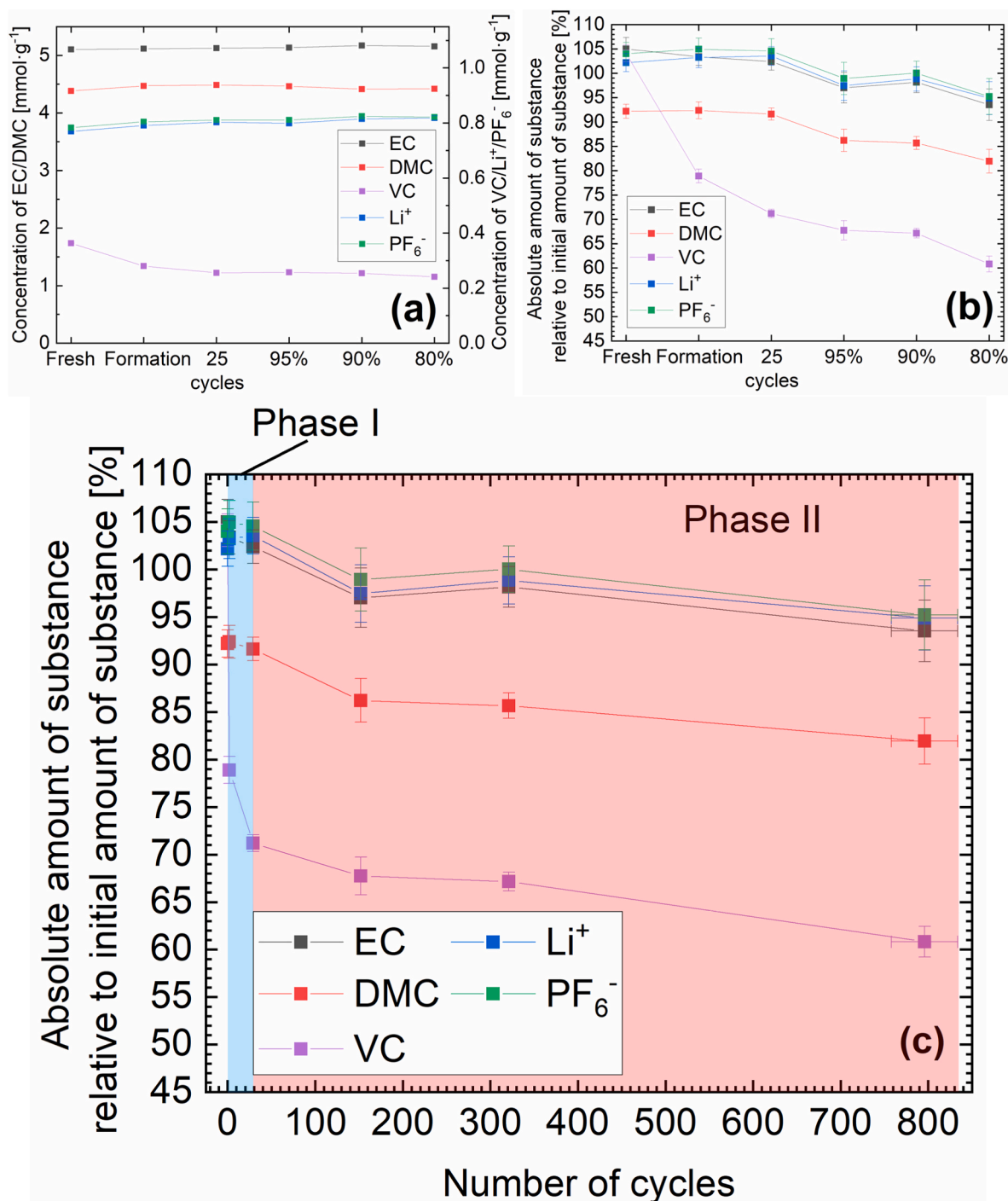


Fig. 1. (a) Relative discharge capacities of the analyzed cells cycled until a remaining capacity of 90% and 80% in dependence on the number of cycles. After every 100 cycles, a checkup cycle is performed with a current of 0.1 C, followed by the determination of the DC internal resistances at various SOCs. (b) DC internal resistance of three cells cycled until a remaining capacity of 80% in dependence on the number of cycles at various SOCs.



**Fig. 2.** (a) Average concentrations of EC, DMC, and VC quantified by HPLC-UV/Vis, as well as the average concentrations of Li<sup>+</sup> and PF<sub>6</sub><sup>-</sup> quantified by HPLC-ESI/MS at selected stages of electrochemical aging. (b/c) Average, relative amounts of substance of EC, DMC, VC, Li<sup>+</sup>, and PF<sub>6</sub><sup>-</sup> in the cells in dependence on the investigated stages of electrochemical aging (b) and on the number of cycles (c). The first phase of electrochemical aging is marked in blue, while the second phase is marked in red (c). The error bars in (a), (b), and (c) are the standard deviations of the mean calculated based on the three single values per indicated, average value. (For interpretation of the references to color in this figure legend, the reader is referred to the Web version of this article.)

DMC, VC, Li<sup>+</sup>, and PF<sub>6</sub><sup>-</sup> during phase I and during phase II, as well as during phase I plus phase II taken together, are shown. In Fig. 3(b), the average, relative electrolyte masses in dependence on the number of cycles are depicted. The relative electrolyte mass corresponds to the quantified electrolyte mass divided by the initial, weighed electrolyte mass in the cell. The quantified electrolyte mass in the cell is determined based on the quantified DEC concentration in the extract and the weighed mass of the DEC injected into the cell.

During formation and the first 25 cycles in phase I, the data in Fig. 3

(a) suggest a preferential decomposition of VC and EC by about 100 μmol, whereas a degradation of DMC, Li<sup>+</sup>, and PF<sub>6</sub><sup>-</sup> cannot be observed in this phase. In literature, a preferential, reductive decomposition of VC in lithium-ion cells on graphite anodes during formation is described [5, 16,17]. Decomposition products of VC, like polymerized VC, deposit on the anode and contribute to the SEI buildup [5,16,17]. A preferential reduction of EC on graphite anodes particularly during the formation associated with SEI buildup is generally known for cells with VC-free electrolytes [18,19]. It is generally accepted that VC suppresses the

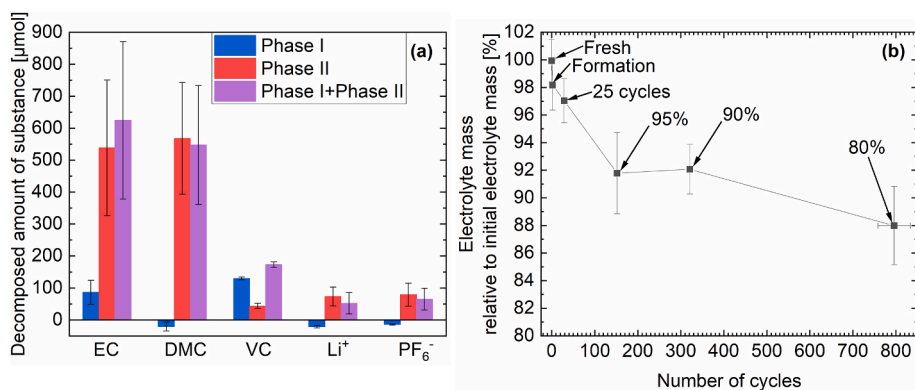


**Fig. 3.** (a) Average, decomposed amounts of substance during formation plus 25 cycles (phase I, blue bars), between the 26th cycle and the about 800th cycle (phase II, red bars), as well as during formation plus about 800 cycles altogether (phase I + phase II, purple bars). A precise description of the calculation of these decomposed amounts of substance can be found in the supplementary information in section S2.1. Each indicated value corresponds to the mean of three single values. The error bars show the associated standard deviation of the mean. (b) Average electrolyte masses in the fresh cells ( $N = 3$ ), the cells after formation ( $N = 3$ ), the cells after 25 cycles ( $N = 3$ ), the cells after cycling until a remaining capacity of 95% ( $N = 3$ ), 90% ( $N = 3$ ), and 80% ( $N = 3$ ) determined by HPLC analyses related to the respective initial electrolyte masses in dependence on the number of cycles. The error bars represent the standard

deviation of the mean calculated by the three single values per shown average value. (For interpretation of the references to color in this figure legend, the reader is referred to the Web version of this article.)

decomposition of the other electrolyte components on graphite anodes during first charging, as it is reduced at higher anode potentials and thus earlier than EC [16]. Nevertheless, the generation of gases associated especially with EC reduction during initial charging was detected in graphite anode/lithium half-cells with VC-containing electrolyte (1 M  $\text{LiPF}_6$  in EC/DMC (1:1 by volume) mixed with 2 wt% VC) by Ota et al. [16]. The gas ethylene suggesting EC reduction were detected in lower amounts in the cells with VC-containing electrolyte than in the cells with VC-free electrolyte after initial charging, but still in substantial amounts [16]. By contrast, methane as specific indicator for DMC reduction, was hardly detected in the VC-containing cells after initial charging [16], suggesting a minor DMC decomposition. These suggestions for a significant VC and EC decomposition during initial charging in literature agrees well with the decomposition of exclusively VC and EC during phase I (see Fig. 3(a)). The reported preferential contribution of EC to the  $\text{Li}^+$  solvation shell compared to DMC and VC [12] might explain the pronounced EC decomposition in phase I. The reduction potential and the composition of the  $\text{Li}^+$  solvation shell influence the preferential solvent reduction [12]. Hence, the preferential VC decomposition might be attributed to the higher reduction potential of VC compared to EC and DMC [12], whereas the preferential EC decomposition might be explained by the dominance of EC in the  $\text{Li}^+$  solvation shell. A decomposition of VC together with EC, as proposed by Ushirogata et al. [11], might be another explanation for the similar consumptions of EC and VC in phase I. It is notable that the preferential decomposition of VC and EC is not only observed during formation, but also during the first 25 cycles. Thus, similar electrochemical decompositions proceed during the first cycles after formation.

During long-term cycling in phase II, the EC and DMC loss is the highest, while the degradation of the other components is clearly slighter (see Fig. 3(a)). The reason for that is a non-preferential decomposition of each electrolyte component to similar extents in phase II (see Fig. 2(c)). Additionally, the initial EC and DMC amounts in the cells are much higher than the initial amounts of  $\text{LiPF}_6$  and VC. Consequently, the decomposed EC and DMC amount is the highest. Indeed, also a significant salt decomposition during long-term cycling in phase II is detectable. During cell aging,  $\text{LiPF}_6$  is known to be decomposed to  $\text{POF}_3$  and lithium fluoride ( $\text{LiF}$ ), a main SEI component, among others [4]. The decomposed amount of substance of VC is distinctly lower in phase II than in phase I (see Fig. 3(a)), suggesting a deceleration of VC degradation and thus possibly other dominating triggers of electrochemical aging and capacity loss during prolonged cycling.

While the relative amounts of substance in Fig. 2(b) and (c), as well as the absolute decomposed amounts of substance in Fig. 3(a) reveal the decomposition of EC, DMC, VC, and  $\text{LiPF}_6$ , the concentrations in Fig. 2(a) indicate just the VC degradation. The reason for this phenomenon is

the continuous decrease of the total electrolyte amount in the cells during formation and cycling, as can be concluded from Fig. 3(b). During formation and cycling, the buildup and growth of surface layers on the electrodes are associated with a continuous electrolyte consumption [3,5,16–18]. Accordingly, the findings in Fig. 3(b) indicate an ongoing reduction of the electrolyte amount in the cells during formation and cycling. This decrease of the electrolyte amount explains, why the concentrations do not provide reliable insight into the real decomposition of the electrolyte [13].

### 3.3. Investigation of the ethylene/methane evolution

To confirm the preferential decomposition of EC in phase I identified by HPLC measurements (see Fig. 3(a)), the evolved amounts of ethylene and methane are analyzed from gas samples of pouch cells after 25 cycles by GC. Ethylene is known to be generated by electrochemical reduction of EC [16,20,21], whereas methane is a known indicator for electrochemical decomposition of DMC [16]. Gas is extracted from a cell after 25 cycles containing the mixed electrolyte (initial electrolyte: LP30 + VC). Besides, gas is also extracted from cells after 25 cycles (at 1 C charge and 1 C discharge rate) each containing either EC electrolyte (initial electrolyte: 1 M  $\text{LiPF}_6$  in pure EC), DMC electrolyte (initial electrolyte: 1 M  $\text{LiPF}_6$  in pure DMC), or VC electrolyte (initial electrolyte: 1 M  $\text{LiPF}_6$  in pure VC). The extracted gases are analyzed by GC-TCD. The peak area ratios ethylene/argon (area of ethylene peak divided by area of argon peak) and methane/argon (area of methane peak divided by area of argon peak) calculated by the chromatograms are a measure for the generated amounts of the respective gases in the cell, as the same argon volume is injected into each cell before extraction. The peak area ratios ethylene/argon and methane/argon for the investigated cells are depicted in Fig. 4.

For the cells with mixed electrolyte and EC electrolyte after 25 cycles, the peak area ratios ethylene/argon are both similar and relatively high (see Fig. 4). In contrast, the peak area ratios ethylene/argon are relatively low for the cell with DMC electrolyte and VC electrolyte (see Fig. 4). The similar values of the peak area ratio ethylene/argon in the cells with mixed electrolyte and EC electrolyte confirm the pronounced EC decomposition in the electrolyte during formation and 25 cycles (see Fig. 3(a)). The peak area ratio methane/argon is high only for the cell with DMC electrolyte after 25 cycles in Fig. 4, as expected. In the cell with mixed electrolyte, no considerable methane amounts are detected, which matches the data in Fig. 3(a) indicating no substantial DMC decomposition during formation and 25 cycles.

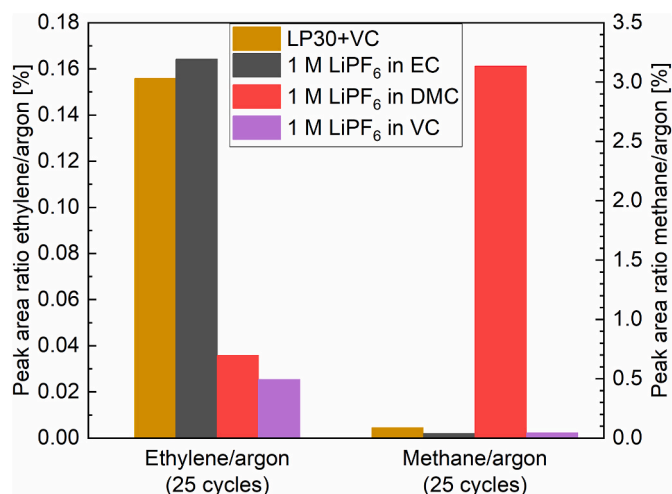


Fig. 4. Peak area ratios ethylene/argon and methane/argon determined by GC-TCD in gas from cells after 25 cycles. The cells are initially filled either with LP30 + VC, 1 M LiPF<sub>6</sub> in pure EC, 1 M LiPF<sub>6</sub> in pure DMC, or 1 M LiPF<sub>6</sub> in pure VC.

### 3.4. Surface analyses of the electrodes by XPS

Electrode surfaces are analyzed by XPS to investigate the composition of the surface layers resulting from the decomposition of the electrolyte components. The investigated electrodes are extracted from a fresh cell, a cell after formation, after 25 cycles, and after cycling until a remaining capacity of 80% each initially filled with LP30 + VC (mixed electrolyte). Additionally, investigated anodes are also extracted from three cells after formation that are initially filled with either 1 M LiPF<sub>6</sub> in pure DMC (DMC electrolyte), 1 M LiPF<sub>6</sub> in pure EC (EC electrolyte), or 1 M LiPF<sub>6</sub> in pure VC (VC electrolyte). The C1s and O1s photoelectron spectra of the investigated anodes are depicted in Fig. 5.

The data in Fig. 5(a) shows that the graphite peak (red) decreases in intensity during formation, which is explained by the buildup of the SEI layer. However, because graphite is still detectable, the SEI is thinner than 5–10 nm (equivalent to the information depth of XPS) after formation. The C<sub>b</sub> peak (291.3 eV, purple) in the C1s spectrum and the O<sub>b</sub> peak (534.5 eV, purple) in the O1s spectrum are detected just on the anode from the cell with the mixed electrolyte and the VC electrolyte after formation (see Fig. 5). In fact, these peaks can be ascribed to polymerized VC (poly(VC)) that represents a major SEI component after formation. Peak assignments of the poly(VC) species are done according to El Ouatani et al. [17]. In literature, poly(VC) is proposed to be the main decomposition product of VC [16,22]. Interestingly, -C-O (286.15 eV), -CO<sub>2</sub> (288.8 eV), and -CO<sub>3</sub> (290.3 eV) species are also observed after formation. When compared to the spectra of electrodes cycled in the DMC electrolyte, EC electrolyte, and VC electrolyte, these three species can be clearly assigned to EC decomposition products (see Fig. 5(c)). Accordingly, -CO<sub>3</sub> groups might be attributed to lithium carbonate, a known component of the SEI formed in EC based electrolytes [23]. Therefore, XPS shows that both VC and EC are decomposed during formation. In the C1s spectrum of the anode after 25 cycles in Fig. 5(a), the graphite peak is has disappeared suggesting the SEI to be thicker than 5–10 nm. Additionally, the peaks ascribed to poly(VC) are absent in the C1s and O1s spectra of the anode after 25 cycles (see Fig. 5(a) and (b)), suggesting VC decomposition to be stronger in early cycling stages. Instead, the intensity of the peaks indicating EC decomposition, i.e. -C-O, -CO<sub>2</sub>, and -CO<sub>3</sub> is increased. The most notable observation in the SEI composition after cycling until a remaining capacity of 80% is the increase in intensity of fluorine-containing SEI components like LiF in the F1s spectra (see Fig. S2(a) in the supplementary information). In fact, XPS indicates for the SEI to be mainly composed of LiF after

long-term cycling, suggesting ongoing salt decomposition upon cycling. A detailed description of the peaks in the spectra shown in Fig. 5 can be found in section S2.2 of the supplementary information.

Electrolyte decomposition also occurs on the cathode, forming the cathode electrolyte interface (CEI). The growth of this layer can be followed in the O1s spectra in Fig. S3(b) in the supplementary information by a continuous decrease of the metal oxide peaks from NCM622. As the NCM622 oxide peak is still visible after prolonged cycling, the emerging surface film is thinner than the XPS probing depth, i.e., 5–10 nm. When comparing electrode/electrolyte interphases on anode and cathode, we can conclude that most of the electrolyte decomposition products are deposited on the anode during formation and long-term cycling.

Overall, XPS identifies poly(VC) as a major SEI component after formation. This suggests for the early SEI to be mainly formed by VC decomposition products, in contrast to later cycling stages, where the poly(VC) component is not detected with XPS. These findings agree with HPLC measurements, which indicate a preferential VC decomposition during formation. EC decomposition products are detected after formation and after 25 cycles, which matches the pronounced EC decomposition during formation and 25 cycles (see Fig. 3(a)). XPS measurements reveal that LiF is the main SEI component after cycling until a remaining capacity of 80%. Contrary to this, HPLC does not indicate LiPF<sub>6</sub> degradation to be dominant, although it reveals slight LiPF<sub>6</sub> decomposition upon long-term cycling, as can be concluded from Fig. 3(a). This difference might result from the fact that with HPLC the global LiPF<sub>6</sub> decomposition is determined, while XPS can only analyze locally the composition of the first 5–10 nm of a spot with 400 μm diameter.

### 3.5. ICP-OES analyses of the electrodes

The content of lithium (Li), manganese (Mn), nickel (Ni), and cobalt (Co) in anodes extracted from a fresh cell, a cell after formation, a cell each after cycling until a remaining capacity of 95%, 90%, and 80% are determined by ICP-OES. To ensure a defined, fully discharged state, each of these cells (except the fresh cell) is discharged to 3 V and held at this voltage for 4 h before the ICP-OES analyses. The initial amount of substance of Li in the cathodes is about 5300 μmol per cell, whereas the initial amount of substance of Li<sup>+</sup> in the electrolyte is about 900 μmol per cell. In Fig. 6, the average, quantified amounts of substance of Li and the transition metals are shown for the investigated anodes (four anode pieces at each cell) at different stages of electrochemical aging.

As explained in section S2.3 in the supplementary information, the irreversible capacity losses are mainly induced by Li trapping in the anodes, respectively the SEI, as described in literature [24]. Thus, a substantial capacity loss by other mechanisms, such as contact loss of NCM622 particles on the cathode side, can be excluded. Summarized, 968 ± 47 μmol additional Li is detected in the anodes after cycling until a remaining capacity of 80%. There are two sources, from which Li could originate: First, “cycleable Li”, which is found within the cathode initially and therefore contributing directly to the capacity. Second, “non-cycleable Li” which is initially found in the electrolyte. With some uncertainties, 818 ± 77 μmol of these 968 ± 47 μmol is cycleable Li, while 52 ± 33 μmol of these 968 ± 47 μmol is non-cycleable Li (see Fig. 3(a)). The irreversible bonding of Li at the anode side is very fast and distinct during formation (see Fig. 6(b)). During cycling, the irreversible bonding of Li slows down with increasing number of cycles.

During formation, no deposition of Mn, Ni, and Co on the anodes can be observed (see Fig. 6(a)). Hence, the distinct, irreversible bonding of Li is not triggered by a deposition of transition metals on the anode during formation. Indeed, the deposited amount of substance of Mn, Ni, and Co on the anodes increases linearly with the number of cycles, as can be seen in Fig. 6(b). Furthermore, the data in Fig. 6 indicate a preferential transfer of Mn from the cathodes to the anodes, as reported in literature [7]. Ni and Mn are admittedly detected in similar amounts in the anodes

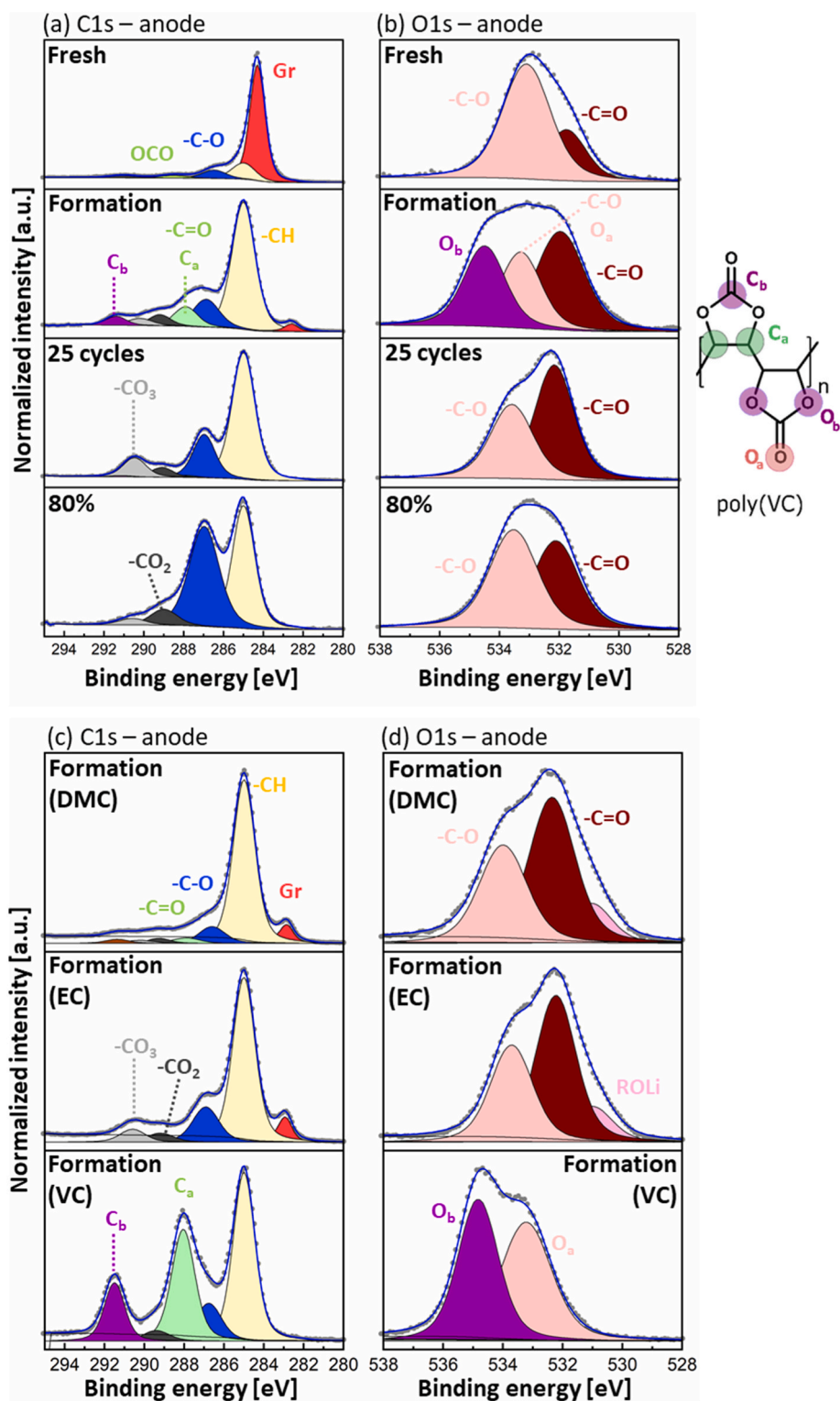


**Fig. 5.** C1s spectra (a) and O1s spectra (b) of anodes from a fresh cell, a cell after formation, after 25 cycles, and after cycling until a remaining capacity of 80% each initially filled with the electrolyte LP30 + VC. Additionally, C1s spectra (c), as well as O1s spectra (d) of anodes from cells after formation that are initially filled with either 1 M LiPF<sub>6</sub> in pure DMC, 1 M LiPF<sub>6</sub> in pure EC, or 1 M LiPF<sub>6</sub> in pure VC, are shown.

(see Fig. 6), but it needs to be considered that the used cathodes with NCM622 as active material contain three times more Ni than Mn. From literature, it is known that transition metals, especially Mn, in the SEI promote electrolyte degradation and capacity loss in lithium-ion cells [7,8,25]. Nevertheless, the irreversible bonding of Li in the anodes is not directly coupled to the deposition of the transition metals, as the

irreversible bonding of Li in the anodes is decelerated with increasing number of cycles, while the amounts of substance of the transition metals increase linearly with the number of cycles. This finding contradicts the observations made by Gilbert et al. in LiNi<sub>0.5</sub>Co<sub>0.2</sub>Mn<sub>0.3</sub>O<sub>2</sub> (NCM523)/graphite coin cells that the Li trapping in the SEI layer is directly linked to the co-deposition of Mn [7]. They concluded that

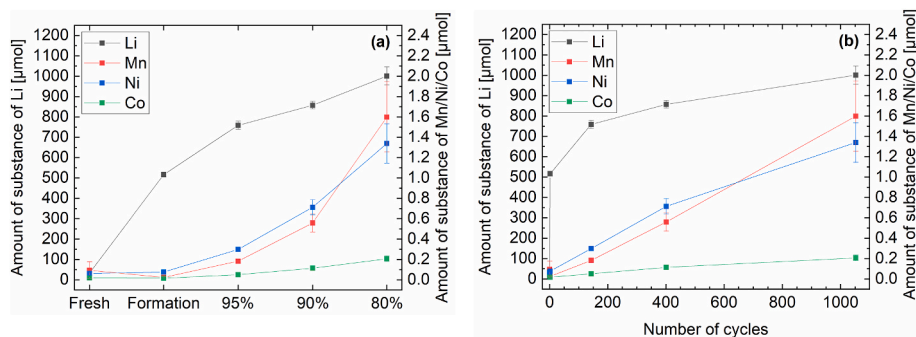


Fig. 6. Amounts of substance of Li, Mn, Ni, and Co in the anodes of a fresh cell, a cell after formation, as well as a cell each after cycling until a remaining capacity of 95%, 90%, and 80% quantified by ICP-OES in dependence on the investigated stages of electrochemical aging (a) and the number of cycles (b). The error bars correspond to the standard deviations of the mean determined based on the four single values per indicated average value.

around 100 extra  $\text{Li}^+$  ions are trapped for every Mn ion in the SEI [7]. As can be concluded from Fig. 6, the amounts of Li additionally trapped in the anodes during cycling are distinctly higher relative to the Mn amounts (around 300 extra Li atoms per Mn atom comparing the cell after formation with the cycled cell with a remaining capacity of 80%). The reason for this discrepancy could be traced back to different cell formats (pouch vs. coin cells), to different cathode active materials (NCM622 vs. NCM523), or presence of additives (VC-containing vs. VC-free electrolyte). Jung et al. stated that capacity fading and loss of cycleable Li by the presence of transition metals in the SEI is reduced

with increasing number of cycles [25]. This agrees with the constant accumulation of transition metals and the simultaneous deceleration of the Li trapping in the anodes during cycling, shown in Fig. 6(b).

### 3.6. Morphology analyses of the electrodes by SEM/EDX

Electrodes from cells in different aging stages are investigated by SEM and EDX. Fig. 7(a) displays SEM images from the separator-facing surface of the anodes. The graphite particles in these images are the big, flake-shaped particles, while the small, dot-like particles are the carbon

(a) SEM images from the anode surfaces

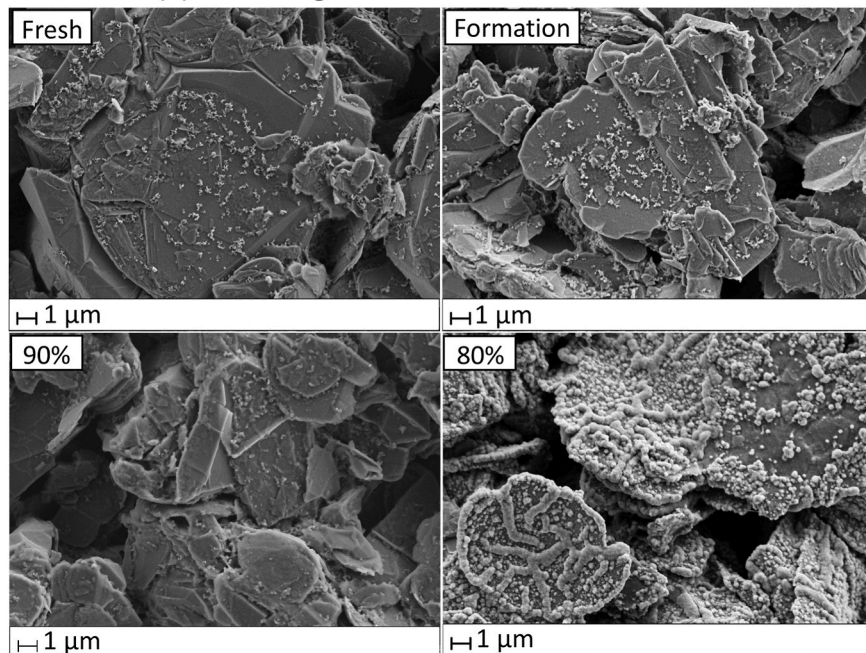
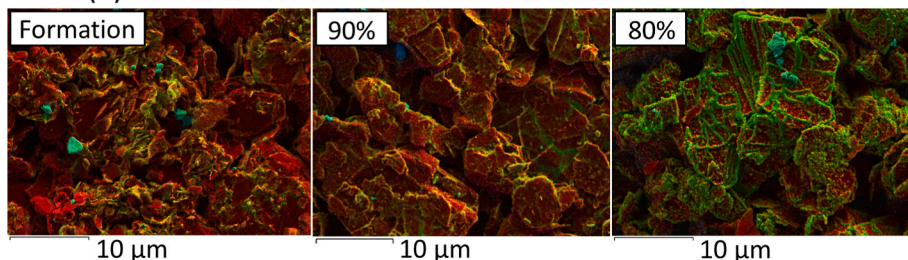


Fig. 7. (a) SEM images from the surface of a fresh anode, an anode after formation, as well as after cycling until a remaining capacity of 90% and 80%. (b) Distribution of the elements on the surface of an anode after formation, as well as after cycling until a remaining capacity of 90% and 80%, determined by EDX analyses. The color green marks spots with a high oxygen concentration, while red marks a high carbon concentration. (For interpretation of the references to color in this figure legend, the reader is referred to the Web version of this article.)

(b) Distribution of the elements on the anode surfaces



black particles visible on the graphite particles. These SEM images indicate no distinct changes of the anode surfaces during formation and cycling until a remaining capacity of 90%. In contrast, the SEM image from the anode surface after cycling until a remaining capacity of 80% shows distinct spherical and tubular deposits on the graphite particles. To gain further information about the origin of these deposits, their elemental composition is analyzed by EDX. Fig. 7(b) shows the distribution of the elements on the surface of anodes in selected aging stages. In Fig. 7(b), high oxygen concentrations in the surface layers are marked in green, whereas high carbon concentrations appear in red. A high oxygen concentration is an indicator for an SEI consisting of decomposition products of EC, DMC, and VC. A high carbon concentration suggests a dominance of graphite in the surface layer and thus the absence of a thick SEI. Thin SEI layers are hardly detectable by EDX due to a limited spatial resolution of several hundred nm. The color cyan in Fig. 7(b) indicates a high aluminum and oxygen concentration that can be attributed to aluminum oxide ( $\text{Al}_2\text{O}_3$ ) from the separator.

Fig. 7(b) indicates a preferential buildup of a thin SEI at the graphite particles edges during formation. The mentioned, spherical and tubular deposits on the graphite particles after cycling until a remaining capacity of 80% appear green (see Fig. 7(b)) and represents thus SEI consisting of decomposition products from EC, DMC, and/or VC. Beside these spherical and tubular deposits on the graphite particles, distinct, oxygen-containing SEI is also visible on the graphite particle edges after long-term cycling in Fig. 7(b), as already observed after formation. The image from the anode after cycling until a remaining capacity of 90% in Fig. 7(b) shows relatively slight deposits on the graphite particles. Nevertheless, beginnings of the mentioned spherical and tubular deposits on the graphite particles are already visible at this stage. From the images in Fig. 7, it can be concluded that most of the decomposition products from the electrolyte are deposited in the later stages of electrochemical aging. This conclusion agrees only partially with the finding indicating a fast electrolyte degradation in the early stages during formation and the first 150 cycles, and a subsequent deceleration (see Figs. 2(c) and Fig. 3(b)). On the other hand, the observed, slight amount of SEI material after formation and the huge amount of SEI material after prolonged cycling in Fig. 7 are consistent with the much stronger electrolyte consumption during long-term cycling than during formation (see Fig. 3(b)).

From literature it is known that the SEI on the basal planes is much thinner than the SEI at the edge of the graphite particles [26–28], which agrees with the observed, preferential SEI buildup at the graphite particle edges in Fig. 7(b). Carbon atoms at the edge sites are reported to have a much higher reactivity than carbon atoms in the basal planes of graphite particles [28], which might explain this phenomenon. The mentioned, spherical deposits on the graphite particles after long-term cycling might be ascribed to a preferential SEI buildup on the carbon black particles that have small sizes and thus large surface areas. Small particle sizes and large surface areas lead to enhanced irreversible capacity loss and associated SEI buildup [28]. The tubular deposits on the basal planes after prolonged cycling in Fig. 7 might be induced by deposited transition metals from the cathode in the SEI, which would match the observed linear increase of the transition metal amounts in the anodes with the number of cycles in Fig. 6(b). Solchenbach et al. proposed that Mn in the SEI leads to the reduction of lithium ethylene dicarbonate, a major SEI component, to lithium carbonate and the gas ethylene associated with cracks in the SEI [8]. These cracks are filled with electrolyte that is reduced, leading to SEI growth [8]. Accordingly, the observed, tubular deposits on the basal planes of the graphite particles after long-term cycling in Fig. 7 might be ascribed to Mn contamination and resulting electrolyte degradation. Another reason for these tubular deposits could be crack formation in the graphite particles by volume changes during lithiation and delithiation, as described in literature [29,30]. The electrolyte in the cracks is known to be reduced at the graphite surface resulting in buildup of new SEI material [29,30]. Thus, the tubular deposits on the graphite particles after prolonged

cycling might have been formed along transgranular cracks, similar to those observed by Harris et al. [31]. To check the appearance of cracks in the graphite particles, SEM images from the cross-sections of the fresh anode and the anode after cycling until a remaining capacity of 80% are recorded, which are pictured in Fig. 8(a). Additionally, these cross-section images are also shown with the distribution of the elements determined by EDX in Fig. 8(a). A high oxygen concentration is marked in green, indicating the presence of a SEI. A high carbon concentration is marked in red. The changes in the cathode during formation and cycling are also investigated by SEM. In Fig. 8(b), the cross-sections of the cathodes in different aging stages are shown.

In Fig. 8(a), a distinct increase of the anode coating thickness can be observed by formation and long-term cycling that can be attributed to the SEI and to an increase of the porosity. The porosity corresponds to the volume ratio of the void space within materials [29]. It is known that

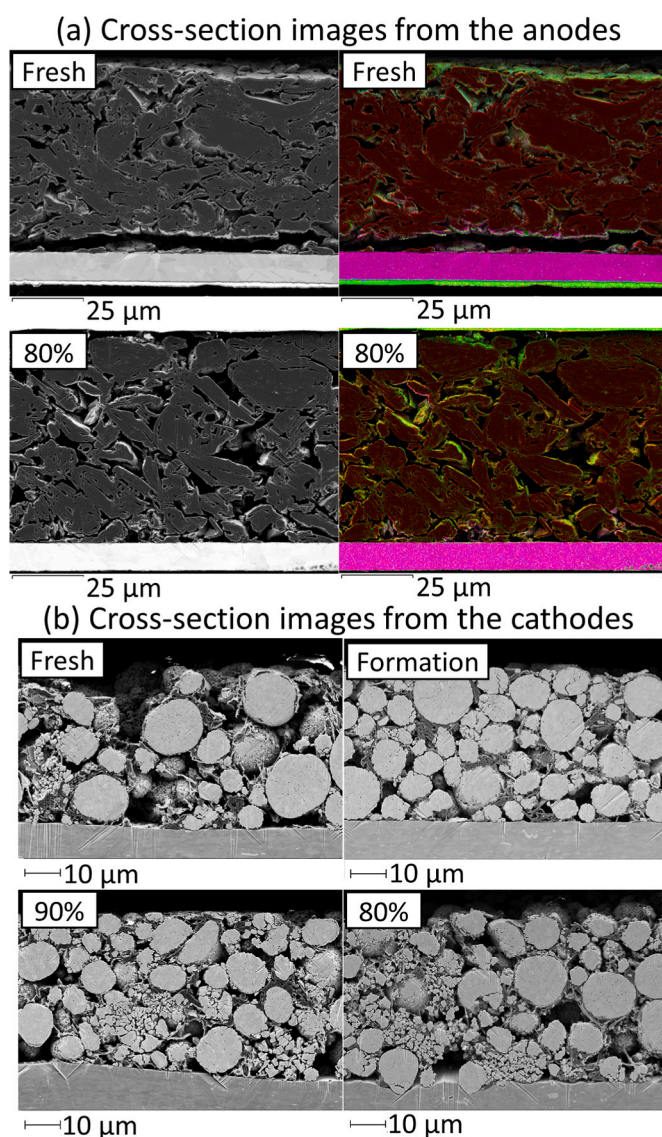


Fig. 8. (a) SEM image from the cross-section of an anode from the fresh cell and of an anode from the cell after cycling until a remaining capacity of 80%. Furthermore, the same images are shown with the distribution of the elements, determined by EDX. The color green marks spots with a high oxygen concentration, while red marks a high carbon concentration. (b) Cross-section images from a cathode of the fresh cell, the cell after formation, the cell after cycling until a remaining capacity of 90%, and 80%, recorded by SEM. (For interpretation of the references to color in this figure legend, the reader is referred to the Web version of this article.)

“the change in porosity before and after electrochemical cycles, which results from crack growth, can be used to quantify the degree of fracture” [29]. Furthermore, oxygen-containing SEI can also be seen partially inside the graphite particles after prolonged cycling in Fig. 8 (a), possibly confirming crack formation and associated electrolyte degradation. This crack formation is plausible, as the cycling of the cells in this study is conducted with high currents. Crack formation is enhanced by high charge and discharge currents due to the higher mechanical stress during cycling [30].

Hence, crack formation due to volume changes of the graphite particles on the one side and transition metal contamination of the SEI on the other side are mainly responsible for the capacity fade and the associated electrolyte decomposition during prolonged cycling. Indeed, it is not obvious, how big the contributions from both mechanisms are.

The image from the cathode of the fresh cell and the cell after formation in Fig. 8(b) show almost no fractures in the spherical NCM622 secondary particles. By contrast, a distinct crack formation is visible in the images from the cathode after cycling until a remaining capacity of 90% and 80% in Fig. 8(b). The lithiation and delithiation of the NCM622 particles is associated with crack formation, leading to an enhanced dissolution of transition metals in the electrolyte [7]. The dissolved transition metals migrate to the anode and deposit in the SEI, accelerating electrolyte decomposition and SEI growth [7,8,25]. Hence, the observed cracks in the NCM622 particles after prolonged cycling in Fig. 8(b) matches the continuous accumulation of the transition metals in the anodes during cycling (see Fig. 6).

#### 4. Conclusions

A comprehensive investigation of electrochemical processes in NCM622/graphite lithium-ion pouch cells initially filled with LP30 + VC during formation and cycling is the objective of this study. For this purpose, a method for electrolyte extraction from pouch cells and subsequent quantitative analyses by HPLC-UV/Vis and HPLC-ESI/MS are used to investigate the absolute consumption of the electrolyte components by electrochemical decomposition. To get a comprehensive insight into the whole cell chemistry during electrochemical aging, complementary analysis methods, namely ICP-OES, XPS, SEM, EDX, and GC, are applied.

Two different phases are identified during cell aging. In phase I, during formation and the first 25 cycles, a thin SEI is built especially at the graphite particle edges by pronounced decomposition of VC and EC. VC is preferentially reduced, since it has a higher reduction potential than EC and DMC. On the other hand, the simultaneous EC decomposition might be ascribed to the dominance of EC in the  $\text{Li}^+$  solvation shell. The VC and EC consumption each by about 100  $\mu\text{mol}$  in phase I is accompanied by a distinct capacity loss mainly through Li trapping in the anodes. In phase I, no DMC and  $\text{LiPF}_6$  decomposition is detected. The relatively high amount of evolved ethylene (indicator for EC reduction) and the relatively low amount of evolved methane (indicator for DMC reduction) in a cell after 25 cycles confirm the pronounced EC decomposition and the electrochemical stability of DMC in phase I. Substantial amounts of poly(VC) and  $-\text{CO}_3$  groups detected on the anodes after formation and after 25 cycles, respectively, can be assigned to VC and EC decomposition products confirming the distinct VC and EC decomposition, as well.

During long-term cycling in phase II (from the 26th cycle until the about 800th cycle), the capacity loss is still induced mainly by Li trapping in the anodes and the SEI grows continuously on the graphite particle edges. Additionally, SEI is now also deposited on the basal planes of the graphite particles in spherical and tubular deposits. The spherical deposits represent SEI formed on the carbon black particles. The tubular deposits might result from SEI cracking (in combination with graphite particle cracking) and consequent SEI rebuilding. Simultaneously, a non-preferential decomposition of the electrolyte components is observed in phase II, meaning EC, DMC, VC, and  $\text{LiPF}_6$  are

decomposed according to their abundance. Hence, EC and DMC are consumed the most by about 500  $\mu\text{mol}$  each, while the VC loss is just about 40  $\mu\text{mol}$ . The decomposed salt amount is moderate with about 70  $\mu\text{mol}$ . Two triggers for the electrolyte decomposition during long-term cycling are identified: On the one hand, there is the progressing SEI contamination with transition metals from the cathode, especially Mn, associated with accelerated electrolyte decomposition. On the other hand, the observed cracks in the graphite particles through volume changes during de-/lithiation might create new electrochemically active graphite surface accompanied by electrolyte reduction and consequent buildup of new SEI.

The determined Li loss of the cathodes during formation and about 800 cycles is around 800  $\mu\text{mol}$  corresponding to about 15% of the initially present Li in the cathodes. Simultaneously, only 50  $\mu\text{mol}$   $\text{Li}^+$  from the electrolyte corresponding to around 6% of the initially present  $\text{Li}^+$  in the electrolyte is lost. Including the uncertainties of the measurements, the sum of both Li losses corresponds to the irreversibly bonded Li on the anode side. The loss of cycleable Li calculated based on the capacity loss during formation and about 800 cycles is around 900  $\mu\text{mol}$  and is thus close to the mentioned Li loss of the cathodes. Hence, most of the capacity loss during formation and long-term cycling can be ascribed to Li trapping in the anodes.

Summarized, these are new findings resulting from this study:

- SEI buildup during formation and the first cycles in electrolytes containing EC and VC is not induced by an (almost) exclusive VC reduction as usually reported, but by a reduction of VC and EC to similar extents.
- SEI growth during long-term cycling is based on a different electrolyte decomposition than SEI buildup, namely a decomposition according to abundance of the components in the electrolyte. Consequently, absolute VC consumption is unexpectedly the lowest during long-term cycling.
- SEI buildup occurs especially on the graphite particle edges, while SEI growth during prolonged cycling additionally proceeds on the basal planes of the graphite particles. In literature, usually a preferential SEI deposition on the graphite particle edges is reported.
- The transition metal amounts in the anode increase linearly with the number of cycles, while electrolyte decomposition and Li trapping in the anode decelerate. Hence, there is no direct correlation between electrolyte consumption and Li trapping on the one hand and the amounts of transition metals in the SEI on the other hand.

Future investigations, for example with Mn-free cells, are necessary to determine the actual contribution of the Mn contamination in the SEI and the crack formation in graphite particles by volume changes during de-/lithiation to electrolyte decomposition and capacity fade upon cell aging.

#### Declaration of competing interest

The authors declare that they have no known competing financial interests or personal relationships that could have appeared to influence the work reported in this paper.

#### Data availability

data is presented in the supporting information

#### Acknowledgements

We thank Sven Leuthner for his support in the cell manufacturing. This work was done at KIT Battery Technology Center (KIT-BATEC) and contributes to the research performed at the Center for Electrochemical Energy Storage Ulm & Karlsruhe (CELEST).

## Appendix A. Supplementary data

Supplementary data to this article can be found online at <https://doi.org/10.1016/j.jpowsour.2022.231842>.

## References

- [1] N. Nitta, F. Wu, J.T. Lee, G. Yushin, Li-ion battery materials: present and future, *Mater. Today* 18 (2015) 252–264, <https://doi.org/10.1016/j.mattod.2014.10.040>.
- [2] L. El Ouatani, R. Dedryvère, C. Siret, P. Biensan, D. Gonbeau, Effect of vinylene carbonate additive in Li-ion batteries: comparison of LiCoO<sub>2</sub>/C, LiFePO<sub>4</sub>/C, and LiCoO<sub>2</sub>/Li<sub>4</sub>Ti<sub>5</sub>O<sub>12</sub> systems, *J. Electrochem. Soc.* 156 (2009) A468, <https://doi.org/10.1149/1.3111891>. –A477.
- [3] R. Fong, U. von Sacken, J.R. Dahn, Studies of lithium intercalation into carbons using nonaqueous electrochemical cells, *J. Electrochem. Soc.* 137 (1990) 2009–2013, <https://doi.org/10.1149/1.2086855>.
- [4] A. Wang, S. Kadam, H. Li, S. Shi, Y. Qi, Review on modeling of the anode solid electrolyte interphase (SEI) for lithium-ion batteries, *Npj Computational Materials* (2018) 1–26, <https://doi.org/10.1038/s41524-018-0064-0>.
- [5] D. Aurbach, K. Gamolsky, B. Markovsky, Y. Gofer, M. Schmidt, U. Heider, On the use of vinylene carbonate (VC) as an additive to electrolyte solutions for Li-ion batteries, *Electrochim. Acta* 47 (2002) 1423–1439, [https://doi.org/10.1016/S0013-4686\(01\)00858-1](https://doi.org/10.1016/S0013-4686(01)00858-1).
- [6] C. Zhan, T. Wu, J. Lu, K. Amine, Dissolution, migration, and deposition of transition metal ions in Li-ion batteries exemplified by Mn-based cathodes – a critical review, *Energy Environ. Sci.* 11 (2018) 243–257, <https://doi.org/10.1039/c7ee03122j>.
- [7] J.A. Gilbert, I.A. Shkrob, D.P. Abraham, Transition metal dissolution, ion migration, electrocatalytic reduction and capacity loss in lithium-ion full cells, *J. Electrochem. Soc.* 164 (2017) A389–A399, <https://doi.org/10.1149/2.1111702jes>.
- [8] S. Solchenbach, G. Hong, A.T.S. Freiberg, R. Jung, H.A. Gasteiger, Electrolyte and SEI decomposition reactions of transition metal ions investigated by on-line electrochemical mass spectrometry, *J. Electrochem. Soc.* 165 (2018) A3304–A3312, <https://doi.org/10.1149/2.0511814jes>.
- [9] N. Kotak, P. Barai, A. Verma, A. Mistry, P.P. Mukherjee, Electrochemistry-mechanics coupling in intercalation electrodes, *J. Electrochem. Soc.* 165 (2018) A1064–A1083, <https://doi.org/10.1149/2.0621805jes>.
- [10] F.A. Soto, Y. Ma, J.M. Martínez de la Hoz, J.M. Seminario, P.B. Balbuena, formation and growth mechanisms of solid-electrolyte interphase layers in rechargeable batteries, *Chem. Mater.* 27 (2015) 7990–8000, <https://doi.org/10.1021/acs.chemmater.5b03358>.
- [11] K. Ushirogata, K. Sodeyama, Y. Okuno, Y. Tateyama, Additive effect on reductive decomposition and binding of carbonate-based solvent toward solid electrolyte interphase formation in lithium-ion battery, *J. Am. Chem. Soc.* 135 (2013) 11967–11974, <https://doi.org/10.1021/ja405079s>.
- [12] S.A. Delp, O. Borodin, M. Olguin, C.G. Eisner, J.L. Allen, T.R. Jow, Importance of reduction and oxidation stability of high voltage electrolytes and additives, *Electrochim. Acta* 209 (2016) 498–510, <https://doi.org/10.1016/j.electacta.2016.05.100>.
- [13] R. Stockhausen, A. Hofmann, L. Gehrlein, T. Bergfeldt, M. Müller, H. Ehrenberg, A. Smith, Quantifying absolute amounts of electrolyte components in lithium-ion cells using HPLC, *J. Electrochem. Soc.* 168 (2021), 080504, <https://doi.org/10.1149/1945-7111/ac1894>.
- [14] K.L. Parry, A.G. Shard, R.D. Short, R.G. White, J.D. Whittle, A. Wright, ARXPS characterisation of plasma polymerised surface chemical gradients, *Surf. Interface Anal.* 38 (2006) 1497–1504, <https://doi.org/10.1002/sia.2400>.
- [15] Y. Qian, C. Schultz, P. Niehoff, T. Schwieters, S. Nowak, F.M. Schappacher, M. Winter, Investigations on the electrochemical decomposition of the electrolyte additive vinylene carbonate in Li metal half cells and lithium ion full cells, *J. Power Sources* 332 (2016) 60–71, <https://doi.org/10.1016/j.jpowsour.2016.09.100>.
- [16] H. Ota, Y. Sakata, A. Inoue, S. Yamaguchi, Analysis of vinylene carbonate derived SEI layers on graphite anode, *J. Electrochem. Soc.* 151 (2004) A1659–A1669, <https://doi.org/10.1149/1.1785795>.
- [17] L. El Ouatani, R. Dedryvère, C. Siret, P. Biensan, S. Reynaud, P. Iratçabal, D. Gonbeau, The effect of vinylene carbonate additive on surface film formation on both electrodes in Li-ion batteries, *J. Electrochem. Soc.* 156 (2009) A103–A113, <https://doi.org/10.1149/1.3029674>.
- [18] D. Aurbach, Y. Ein-Eli, B. Markovsky, A. Zaban, S. Luski, Y. Carmeli, H. Yamin, The study of electrolyte solutions based on ethylene and diethyl carbonates for rechargeable Li batteries: II. Graphite electrodes, *J. Electrochem. Soc.* 142 (1995) 2882–2890, <https://doi.org/10.1149/1.2048659>.
- [19] H. Yoshida, T. Fukunaga, T. Hazama, M. Terasaki, M. Mizutani, M. Yamachi, Degradation mechanism of alkyl carbonate solvents used in lithium-ion cells during initial charging, *J. Power Sources* 68 (1997) 311–315, [https://doi.org/10.1016/S0378-7753\(97\)02635-9](https://doi.org/10.1016/S0378-7753(97)02635-9).
- [20] R. Imhof, P. Novák, In situ investigation of the electrochemical reduction of carbonate electrolyte solutions at graphite electrodes, *J. Electrochem. Soc.* 145 (1998) 1081–1087, <https://doi.org/10.1149/1.1838420>.
- [21] B. Zhang, M. Metzger, S. Solchenbach, M. Payne, S. Meini, H.A. Gasteiger, A. Garsuch, B.L. Lucht, Role of 1,3-propane sultone and vinylene carbonate in solid electrolyte interface formation and gas generation, *J. Phys. Chem. C* 119 (2015) 11337–11348, <https://doi.org/10.1021/acs.jpcc.5b00072>.
- [22] M. Nie, J. Demeaux, B.T. Young, D.R. Heskett, Y. Chen, A. Bose, J.C. Woicik, B. L. Lucht, Effect of vinylene carbonate and fluoroethylene carbonate on SEI formation on graphitic anodes in Li-ion batteries, *J. Electrochem. Soc.* 162 (2015) A7008–A7014, <https://doi.org/10.1149/2.0021513jes>.
- [23] P. Verma, P. Maire, P. Novák, A review of the features and analyses of the solid electrolyte interphase in Li-ion batteries, *Electrochim. Acta* 55 (2010) 6332–6341, <https://doi.org/10.1016/j.electacta.2010.05.072>.
- [24] Y. Li, M. Bettge, B. Polzin, Y. Zhu, M. Balasubramanian, D.P. Abraham, Understanding long-term cycling performance of Li<sub>1.2</sub>Ni<sub>0.15</sub>Mn<sub>0.55</sub>Co<sub>0.1</sub>O<sub>2</sub>-graphite lithium-ion cells, *J. Electrochem. Soc.* 160 (2013) A3006–A3019, <https://doi.org/10.1149/2.002305jes>.
- [25] R. Jung, F. Linsenmann, R. Thomas, J. Wandt, S. Solchenbach, F. Maglia, C. Stinner, M. Tromp, H.A. Gasteiger, Nickel, manganese, and cobalt dissolution from Ni-rich NMC and their effects on nmc622-graphite cells, *J. Electrochem. Soc.* 166 (2019) A378–A389, <https://doi.org/10.1149/2.1151902jes>.
- [26] J. Asenbauer, T. Eisenmann, M. Kuenzel, A. Kazzazi, Z. Chen, D. Bresser, The success story of graphite as a lithium-ion anode material – fundamentals, remaining challenges, and recent developments including silicon (oxide) composites, *Sustain. Energy Fuels* 4 (2020) 5387–5416, <https://doi.org/10.1039/d0se00175a>.
- [27] D. Bar-Tow, E. Peled, L. Burstein, A study of highly oriented pyrolytic graphite as a model for the graphite anode in Li-ion batteries, *J. Electrochem. Soc.* 146 (1999) 824–832, <https://doi.org/10.1149/1.1391688>.
- [28] E. Peled, S. Menkin, Review—SEI: past, present and future, *J. Electrochem. Soc.* 164 (2017) A1703–A1719, <https://doi.org/10.1149/2.1441707jes>.
- [29] P. Li, Y. Zhao, Y. Shen, S.-H. Bo, Fracture behavior in battery materials, *J. Phys. Energy* 2 (2020), 022002, <https://doi.org/10.1088/2515-7655/ab83e1>.
- [30] N. Lin, Z. Jia, Z. Wang, H. Zhao, G. Ai, X. Song, Y. Bai, V. Battaglia, C. Sun, J. Qiao, K. Wu, G. Liu, Understanding the crack formation of graphite particles in cycled commercial lithium-ion batteries by focused ion beam - scanning electron microscopy, *J. Power Sources* 365 (2017) 235–239, <https://doi.org/10.1016/j.jpowsour.2017.08.045>.
- [31] S.J. Harris, R.D. Deshpande, Y. Qi, I. Dutta, Y.-T. Cheng, Mesopores inside electrode particles can change the Li-ion transport mechanism and diffusion-induced stress, *J. Mater. Res.* 25 (2010) 1433–1440, <https://doi.org/10.1557/JMR.2010.0183>.